RESEARCH ARTICLE | APRIL 15 2026

Infrared-laser-induced Marangoni flow programs ice-melting patterns

Yuqi Li ; Man Hu ; Feng Wang; Li Chen ; Wenna Wu; Peng Huo; Xi Gu ; Daosheng Deng

Physics of Fluids 38, 042113 (2026)
https://doi.org/10.1063/5.0325486

Infrared-laser-induced Marangoni flow programs ice-melting patterns

Cite as: Phys. Fluids **38**, 042113 (2026); doi: 10.1063/5.0325486
Submitted: 30 January 2026 · Accepted: 24 March 2026 ·
Published Online: 15 April 2026

Yuqi Li, Man Hu,[a] Feng Wang, Li Chen, Wenna Wu, Peng Huo, Xi Gu, and Daosheng Deng[b]

AFFILIATIONS

Department of Aeronautics and Astronautics, College of Intelligent Robotics and Advanced Manufacturing, Fudan University, Shanghai 200433, China

[a]Electronic mail: human@fudan.edu.cn
[b]Author to whom correspondence should be addressed: dsdeng@fudan.edu.cn

ABSTRACT

Climate-driven ice loss from glaciers and icebergs exacerbates sea-level rise and freshwater scarcity, yet the role of radiative forcing in regulating melt dynamics remains poorly understood. Here, we investigate ice-melting patterns under mid-infrared (10.6 μm) CO_2 laser irradiation by combining experimental approaches, numerical simulations, and scaling analysis. We observe the spatiotemporal evolution of melt ponds transitioning from concave to anomalous convex morphologies, driven by thermal Marangoni flows at the ice–water interface. Melt pond patterns can be precisely controlled through premelting liquid layers (which favor convex patterns), laser power, or laser operation modes (e.g., scanning mode for groove-shaped channels). At higher laser intensities, vaporization and bubble dynamics significantly influence ablation processes, replicating feedback mechanisms observed in natural ice–ocean systems such as marine ice cliff instability. Our findings not only demonstrate the potential of radiative interventions for managing meltwater dynamics but also establish a crucial link between microscale phase-change physics and macroscale ice-sheet responses, offering actionable insights for mitigating freshwater loss under global climate change.

I. INTRODUCTION

Ice in nature, spanning from icebergs to ice sheets, covers nearly one-tenth of Earth's surface and serves as a vital freshwater reserve, storing approximately 70% of the planet's freshwater, primarily in regions such as Greenland and Antarctica.[1–4] Over the past two decades, accelerated by climate change and global warming, the rapid melting and mass loss of glaciers worldwide have exacerbated sea-level rise and compromised coastal resilience.[5–11] To mitigate ice loss and preserve glacial systems, intervention strategies such as glacier covering, artificial snow production, water injection, and radiative cooling materials have been implemented.[12–14] However, these approaches face challenges in scalability and long-term efficacy, underscoring the critical need for a deeper understanding of ice-melting processes, and such insights are essential to develop adaptive strategies that address sea-level impacts and safeguard global water resources in a warming climate.

From a fundamental scientific perspective, ice melting is often simplified as a classical Stefan problem,[15,16] yet it is in fact an extraordinarily complex process involving multiphysics coupling—spanning heat transfer, phase transitions, hydrodynamic flow, and ambient environmental interactions—across scales from pore-sized brine percolation to ice-sheet hydrofracture.[17–22] Consequently, these coupled interactions generate emergent, often intricate morphologies and dynamic patterns.[23] For instance, submerged ice develops pinnacles and scallops under convective flows driven by the 4 °C density anomaly of water, which creates unstable stratification.[24] Ice–water systems further exhibit diverse flow regimes governed by ice-front geometry and stratified boundary layers, modulated by thermophysical properties such as latent heat exchange and density gradients.[25–27] Notably, the release of trapped bubbles accelerates localized melting rates by enhancing turbulent kinetic energy fluxes and buoyancy-driven mixing, introducing nonlinear feedback into ablation processes.[28]

Despite significant advancements in understanding ice-melting dynamics, the role of solar radiative heating—the primary driver of melt pond formation—remains underexplored. This critical gap traces back to foundational work by John Tyndall in the 1850s, who first examined ice melting under solar radiation during clear-sky conditions, observing inverse snowflake-like water structures.[29–32] Recent studies demonstrate that near-infrared (1540 nm) illumination, strongly absorbed by ice, generates labyrinthine melt patterns in aqueous sucrose solutions, revealing a self-organizing interplay between spectral absorption and hydrodynamic instabilities.[33] Geometric

models employing overlapping circular voids have further been proposed to explain the spatial heterogeneity of Arctic melt ponds,[34] while simulations identify bistable morphologies governed by nonlinear couplings between radiative heat transfer and convective ablation.[35] Collectively, these works underscore the complexity of radiative ice interactions, yet a systematic framework linking spectral heating to emergent melt geometries, particularly under controlled irradiation mimicking solar forcing, remains elusive, hindering predictive models of ice-sheet vulnerability.

In addition, as global climate change progresses and polar resource exploration advances, the development of efficient deicing and icebreaking technologies becomes crucial for ensuring the safety and efficiency of polar navigational routes.[36] In recent years, laser technology, as an efficient and non-contact deicing method, has made significant advancements in the fields of deicing and icebreaking. Experimental studies on the melting and drilling effects of CO_2 lasers on ice delve into the deicing mechanisms under different irradiation intensities, ice densities, and beam angles.[37–39] However, CO_2 laser deicing technology has not been fully studied, especially the physical mechanism of radiative heat transfer and convection in melt ponds.

In this work, we investigate ice-melting dynamics by irradiating transparent ice cubes with a mid-infrared 10.6 μm CO_2 laser, enabling direct observation of spatiotemporal melt-pattern evolution. By leveraging the optical transparency of ice, we reveal microscopic mechanisms governing these dynamics, including hydrodynamic flow regimes and thermal gradients. Our experiments identify melt ponds transitioning from concave to anomalous convex morphologies, driven by thermal Marangoni flows at the ice–water interface. Melt pond geometry is precisely controlled through two distinct strategies: premelting liquid layers (which promote convex patterns) and laser scanning modes (which generate groove-shaped channels reminiscent of those observed in additive manufacturing). At elevated laser intensities, vaporization and bubble dynamics perturb ablation processes, replicating feedback mechanisms observed in natural ice–ocean systems, such as marine ice cliff instability. These findings not only demonstrate the potential of radiative interventions to modulate meltwater dynamics but also bridge microscale phase-change physics with macroscale ice-sheet responses, thereby informing mitigation strategies for freshwater loss in the context of global climate change. Furthermore, these findings provide a deeper understanding of the ice-melting process under laser irradiation and serve as a reference for the optimization of CO_2 laser ice-melting technology.

II. EXPERIMENTAL SETUP

For ice cube sample preparation, de-ionized water is first degassed by heating to boiling. Then, the degassed de-ionized water is stored in an open container ($5 \times 5 \times 5\,cm^3$ PMMA) wrapped with a layer of insulating material (plastic foam) and cooled in a refrigerator at $-15\,^{\circ}C$ over 24 h. Due to the single-direction cooling process, the frozen ice is highly transparent without bubbles.

The experimental setup is shown in Fig. 1. The ice is impacted from the top by a laser source with 10.6 μm wavelength, a power of 20 W, and a beam diameter of about 3 mm. The dynamics of the melt pond are captured by a high-speed camera at a frame rate of 125 Hz (Phantom V611). The temperature evolution of the melt pond is acquired by an infrared thermal camera at a frame rate of 125 Hz (FLIR A6750sc).

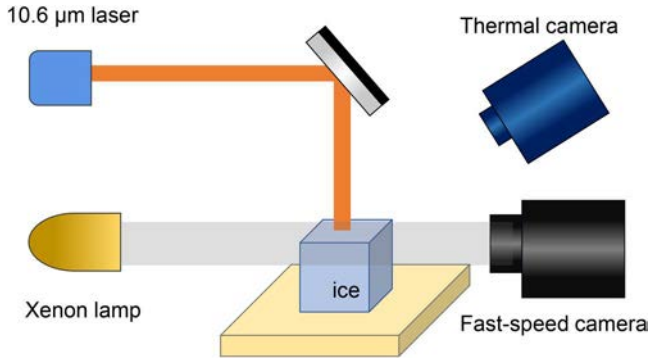

FIG. 1. Sketch of the experimental setup.

III. PATTERN EVOLUTION FROM A CONCAVE CRATER TO A CONVEX CRUST

When a continuous 10.6 μm laser with a Gaussian-profile intensity impacts ice [Fig. 2(a)], due to the strong absorption coefficient of 1580 and 870 cm^{-1} for ice and water,[40–43] the rapid deposition of laser energy results in localized violent vaporization. As the vapor is ejected upward into the air, liquid is pushed downward by overcoming surface tension to form a crater, an air–water depression, as shown in Fig. 2(b) (Multimedia view). The morphology of the crater and the melt pond is characterized by the air–water interface (the yellow line) and the water–ice interface (the red line).

In previous work on near-infrared irradiation, a 1064 nm laser beam at an intensity of 180 W/m^2 was used to create microchannels,[44] and 1540 nm laser illumination at an intensity of 14 W/cm^2 formed a labyrinth ice pattern.[33] Since the absorption coefficient of ice and water in the mid-infrared is two or three orders of magnitude larger than that at near-infrared wavelengths, both the strong absorption at the mid-infrared wavelength of 10.6 μm and the high laser intensity of 280 W/cm^2 contribute to the generation of the crater and melt pond in the ice.

Corresponding to the Gaussian profile of the stationary laser beam intensity, the crater is characterized by a nearly semi-spherical air–water interface, while the propagation of the melting front at the central part is faster, resulting in a concave ice–water interface. At a later stage ($t = 0.96$ s), as more ice melts, the melt pool enlarges with more water. Simultaneously, the heat accumulated within the pool is rapidly dissipated into the surrounding water, ice, and air via heat transfer. Consequently, the recoil pressure from evaporation becomes insufficient to sustain the concave air–water interface. The previously formed crater collapses, and the air–water interface eventually becomes nearly flat. Subsequently, the melting front or the ice–water interface has been transformed from a concave to convex shape [Figs. 2(a) and 2(c)]. This anomalous convex shape of the melt pond is distinct from the concave morphology, as the central part of melting front becomes slower, which is opposed to the expectation of a faster melting front at a higher temperature according to the laser intensity distribution of a Gaussian beam.

Quantitatively, the morphology evolution of the crater and the melt pond is presented [Figs. 3(a)–3(c)]. The depth of the crater at the air–water interface (d_{aw}) and that of the melt pond at the water–ice

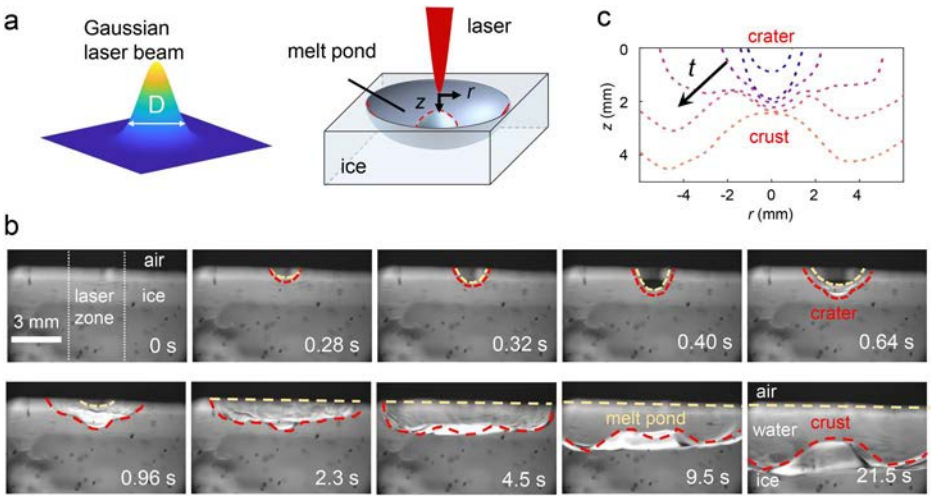

FIG. 2. Melt pond shape evolves from a concave crater to a convex crust. (a) Sketch of the Gaussian-profile laser intensity and the anomalous convex melt pond in ice. (b) High-speed side-view images of the melt pond impacted a 10.6 μm laser ($P = 20$ W, $D_{laser} = 3$ mm) on the ice at the initial surface temperature ($T_0 = 0.1\,^{\circ}$C). Orange lines and red lines correspond to the air–water interface and the water–ice interface, respectively. (c) Time-evolution of melting front or the water–ice interface, illustrating the morphological transition of the melt pond from a concave to convex shape. Multimedia available online.

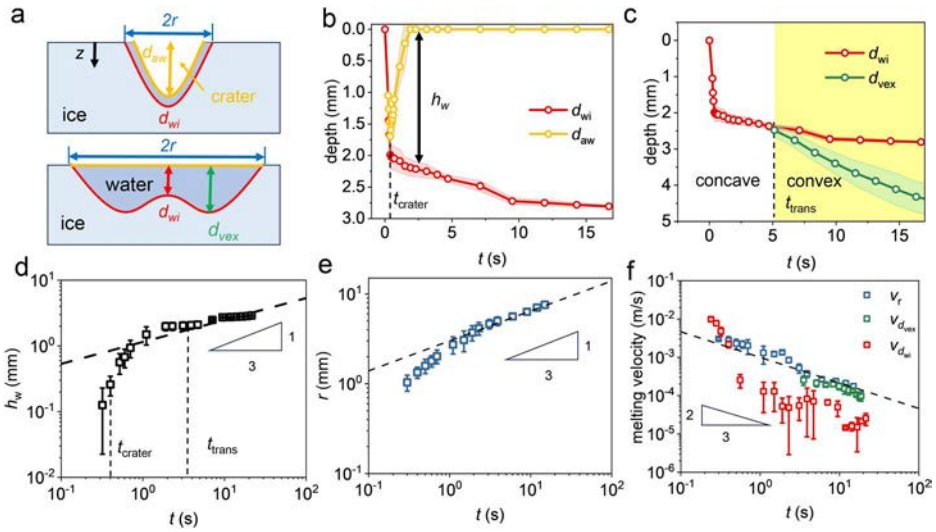

FIG. 3. Spatiotemporal evolution of the melt pond. (a) Sketch of the geometric parameters: r is the radius, d_{aw}, d_{wi} are the central depth of the air–water interface and the water–ice interface, while d_{vex} is the depth of the convex profile. (b) and (c) Time-dependent central depth of d_{aw}, d_{wi}, and d_{vex}. (d) and (e) Thickness of water layer h_w and radius r following a $1/3$ scaling law with time. (f) Velocity of melting front v_r, v_{wi}, and v_{vex} following a $-2/3$ scaling law with time in the late stage.

interface (d_{wi}) are presented in Fig. 3(b). Initially, due to pronounced vaporization, both d_{aw} and d_{wi} increase rapidly until $t_{crater} = 0.4$ s, and the crater is formed. After t_{crater}, the crater collapses, and the melting front continues growing slowly and reaches 2.5 mm at 15 s. From the difference of these two depths, the thickness of water ($h_w = d_{wi} - d_{aw}$) is obtained [Fig. 3(d)].

As shown in Fig. 3(c), the shape of the melt pond transforms from a concave to a convex morphology at $t_{trans} = 4.5$ s. Before t_{trans}, the melt pond remains concave shaped, and its central depth (d_{wi}) increases with time while the width r of the melt pond gradually expands. After t_{trans}, a pronounced convex shape is observed, and its characterized depth d_{vex} reaches 5 mm at 15 s.

Despite the complicated heat transfer process, the melting of ice is driven by energy from laser irradiation. As the melt pond radius grows substantially larger than the laser beam diameter (3 mm), the laser is treated as a radial point heat source. The melt pool is assumed to be hemispherical and dominated by thermal diffusion, with ice melting occurring in both radial and axial directions. Under continuous laser illumination, the energy consumed at the melting front in the late stage [i.e., at the location indicated by the entire red dotted curves in the lower panel of Fig. 2(b)] is approximately constant,

$$(\rho L_m v) r^2 \sim const \quad (v = dr/dt). \tag{1}$$

Here ρ, L_m, v are the density of water, the specific latent heat of melting from ice to water, and the velocity at the melting front, respectively. Then, the following scaling laws are obtained:

$$r \propto t^{1/3}, \quad v \propto t^{-2/3}. \tag{2}$$

Indeed, this $1/3$ scaling of length (h_w, r) and $-2/3$ scaling of velocity (v_r, v_{iw}, v_{vex}) are in reasonable agreement with the experiment data in the late stage [Figs. 3(d)–3(f)].

IV. MECHANISM OF THE ANOMALOUS CONVEX CRUST

The spatiotemporal evolution of temperature at the surface or the air–water interface is captured by thermal images from the top-down view [Fig. 4(a), Multimedia view]. Initially, corresponding to the laser intensity, the temperature of the melt pond decreases monotonically from the center to the circular rim. Then, flows on the surface of the melt pond appear, and the circular symmetry of the rim is broken, leading to irregular patterns. Clearly, the water surface in the melt pond is in a superheated state, and this peak temperature at the center gradually decays with time [Fig. 4(b)].

By taking advantage of the transparency of ice and water, particle image velocimetry (PIV) measurement is employed to check the internal flow within the melt pond from the side view [Fig. 4(c), Multimedia view]. For PIV measurement, after the molten pond is formed by laser irradiation of ice, the laser is paused, and 10 μm SiO_2 particles are added into the melt pond. Then, the laser is turned on, and the particle trajectories are captured by a high-speed camera at a 400 Hz frame rate. The velocity of the circulation flow at the surface can be on the order of 0.1 m/s as determined by particle tracing, which is comparable to the estimated thermal Marangoni velocity or thermocapillary velocity u_{th},[45]

$$u_{th} = \frac{\Delta T|\partial\gamma/\partial T|H}{\eta R} \sim 10^{-1}\ \text{m/s}. \tag{3}$$

Here, $H = 10^{-3}$ m and $R = 10^{-2}$ m are the characteristic thickness and radius of the melt pond, respectively; $\eta = 10^{-3}$ Pa s is the viscosity of water; and $|\partial\gamma/\partial T| = 1.4 \times 10^{-4}$ N/(m K), where γ is the surface tension, $\Delta T = 10$ K is the characteristic temperature difference at the air–water interface. The radial flows varying along the z-axis [Fig. 4(d)] show an outward flow in the upper part of the melt pond and an inward flow in its lower part, with the velocity on the order of 0.03 m/s, indicating a recirculation flow inside the melt pond.

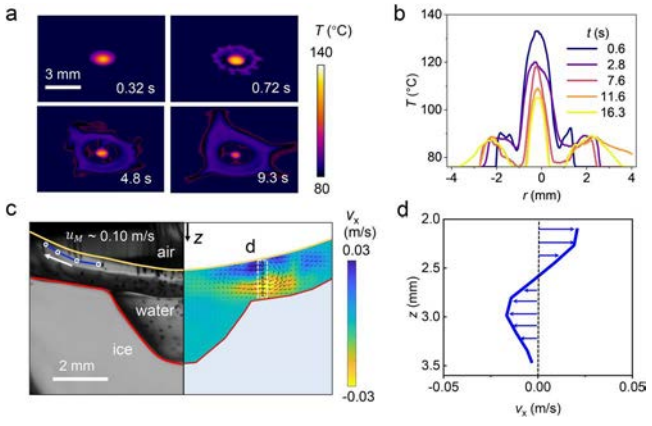

FIG. 4. Temperature distribution and flow field. (a) Thermal images of the melt pond from top-down view. (b) Temperature evolution along a centerline. (c) Side-view snapshot of the melt pond by particle tracking (left) and PIV (right). (d) Horizontal velocity of the internal flow as a function of depth, indicating a recirculation flow. Multimedia available online.

In order to understand the transition from the concave shape to the convex profile at the melting front, we take into account thermocapillary convection in the heat transfer. Particularly, the dimensionless Péclet number is applied to compare the conduction mode and convection mode within the melt pond,

$$Pe = \frac{h_w u_{th}}{\alpha}, \tag{4}$$

where $u_{th} = O(10^{-2}) \sim O(10^{-1})$ m/s is the typical thermocapillary velocity, h_w is the thickness of water for the liquid layer, and $\alpha = \kappa/(\rho c_p) = 1.4 \times 10^{-7}$ m^2/s is the thermal diffusivity of water (κ, c_p, ρ are the thermal conductivity, the specific heat, and the density of water, respectively, see supplementary material Table I).

At the initial stage ($t < t_{crater}, h_w = 0.1$ mm), as laser energy is absorbed by ice, ice undergoes a phase transition and melts into water, which subsequently undergoes rapid vaporization. However, at later stages ($t > t_{crater}, h_w = 2$ mm), due to the increased h_w and the elevated temperature ΔT, the increased $\text{Pe} = O(10^2) \sim O(10^3)$ implies heat convection becomes significant.

As the liquid is further illuminated by the laser, the temperature of water is further elevated, and thermocapillary convection is triggered at the air–water interface. Due to the negative surface tension coefficient of water ($\partial\gamma/\partial T < 0$), water on the surface of the melt pond flows from higher-temperature regions (at the center of the laser zone or the rim of the melt pond) to lower-temperature regions (the periphery or edge of the melt pond). In this fashion, two recirculation vortices accompanying this thermocapillary convection (or thermal Marangoni convection) appear in the melt pond, which subsequently affect the heat transfer and significantly sculpt the water–ice interface to produce the anomalous convex melting front.

V. EFFECT OF PREMELTING ICE

This systematic understanding of the melt pond provides insight into the modification of the melt pond by adjusting physical parameters. This anomalous convex melt pond is determined by the strong recirculation flow, which is sensitive to both heat transfer and thermocapillary convection. Since the premelting liquid layer under laser illumination enhances thermal convection via the thermal Marangoni effect at the air–liquid interface, the convex shape has a greater tendency to form.

Hence, here we investigate the effect of a premelting water layer[46] by considering two cases [Fig. 5(a), supplementary material Note 3]. The initial ice at a high surface temperature $T_0 = 0.1\,^\circ$C is covered by the premelting water layer [Fig. 5(b), top panel] or at a low surface temperature $T_0 = -6.8\,^\circ$C remains dry [Fig. 5(b), bottom panel], while all the other parameters such as the laser power remain the same. In experiments, by slightly changing the initial ice surface temperature, we find the distinctive morphologies of the melt pond, either a convex profile or a convex shape [Fig. 5(b)]. With the premelting liquid layer at $T_0 = 0.1\,^\circ$C, a noticeable protrusion has occurred for a convex water–ice interface at $t = 9$ s [Fig. 5(b), top panel]. Conversely, for the dry ice surface without a premelting liquid layer at $T_0 = -6.8\,^\circ$C, the melting surface shape is still concave [Fig. 5(b), bottom panel, Multimedia view]. Initially, both melt ponds show rapid deepening. The melt pond with $T_0 = 0.1\,^\circ$C reaches a depth of $d_{wi} \approx 2$ mm at $t_{crater} = 0.4$ s, but the melt pond at $T_0 = -6.8\,^\circ$C continues to deepen until $d_{wi} = 4.5$ mm

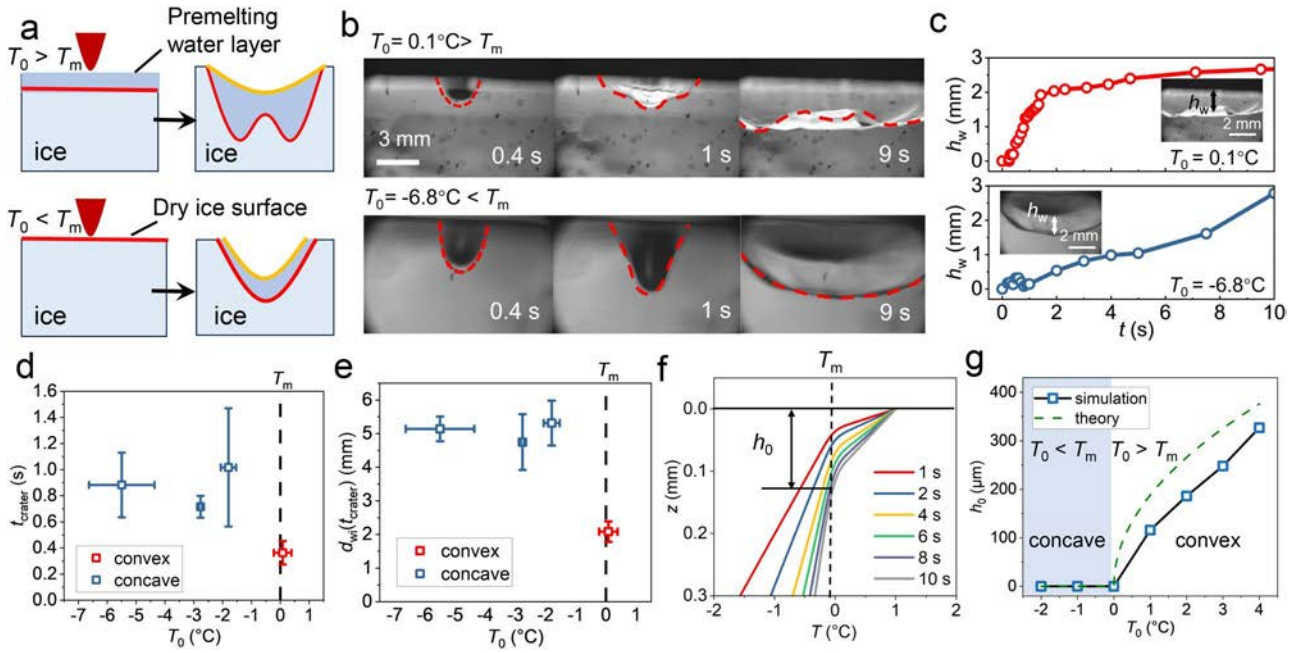

FIG. 5. Effect of the initial surface temperature (T_0) on melt pond. (a) Sketch of the convex melt pond with a wet surface or premelting liquid layer at a high initial surface temperature ($T_0 > T_m$), and the concave melt pond with a dry surface at a low initial surface temperature ($T_0 < T_m$). (b) Side-view images of the melt pond at $T_0 = 0.1$ and $-6.8\,^\circ$C. (c) Dynamics of the thickness of water layer h_w at $T_0 = 0.1$ and $-6.8\,^\circ$C. (d) t_{crater} at different T_0. (e) Melt pond depth, $d_{wi}(t_{crater})$, at t_{crater} for various T_0. (f) 1D simulation of temperature distribution for a semi-infinite-thickness ice with time (at $T_0 = 1\,^\circ\text{C} > T_m$). (g) 1D two-phase Stefan theory and simulation for the characteristic thickness of premelting liquid film h_0 (at $t = 10$ s) for various surface temperatures T_0. Multimedia available online.

at $t_{crater} = 1$ s. The dynamics of h_w with different initial surface temperatures T_0 are also compared in Fig. 5(c). h_w of the melt pond with $T_0 = 0.1\,^\circ$C increases from 0.1 to over 1 mm rapidly at $t_{crater} = 0.4$ s, while h_w of the melt pond with $T_0 = -6.8\,^\circ$C increases slowly after $t_{crater} = 1$ s.

Through more systematic experiments for different initial temperatures T_0 ranging from -6.8 to $0.4\,^\circ$C, we further demonstrate the robustness of the determination of the ice melt pond shape by the initial ice surface temperature. According to the shape of melt ponds at $t = 10$ s, the melt ponds can be divided into two types: convex and concave. Figures 5(e) and 5(f) show that when the initial surface temperature is near the melting point T_m, melt ponds are convex and will reach a depth of $d_{wi} \approx 2$ mm at $t_{crater} = 0.3$ s. On the contrary, once the initial surface temperature is much below T_m (in our experiment, the highest T_0 of the concave melt pond is $-1.5\,^\circ$C), the depth of the melt pond can continue increasing to $d_{wi} \approx 5$ mm at $t_{crater} = 1$ s. Both t_{crater} and $d_{wi}(t = t_{crater})$ concave melt ponds are nearly 2 to 3 times as large as those of convex melt ponds.

To quantify the thickness of the premelting liquid film, we build a 1D theory based on a two-phase Stefan model for a semi-infinite-thickness ice, and perform a 1D simulation for the evolution of temperature for a finite-thickness ice [Fig. 5(f), supplementary material Note 1]. At a high surface temperature $T_0 = 1\,^\circ\text{C} > T_m$, the thickness of the premelting water layer of ice increases with time as $h = 2\sqrt{Dt}$ [with diffusion coefficient $D = 2k_w(T_m - T_0)/\rho_w L_m$],[45] and exceeds 100 μm at 10 s. The characteristic thickness of the premelting liquid film (h_0) will reach $O(10) \sim O(10^2)$ μm at $T_0 > T_m$ [Fig. 5(g)], three orders of magnitude larger than the nanometer-scale premelting layer at $T_0 = -6.8\,^\circ$C.[46]

VI. EFFECT OF LASER POWER

Furthermore, we experimentally investigate the effect of laser power on the morphology of the melt pond. For the given initial surface temperature $T_0 \approx 0.8\,^\circ$C, as the laser power increases, T_{peak} increases with laser power [Fig. 6(a)], and three distinct modes of the melt pond shape evolution have been identified [Fig. 6(b)]. At a lower power density of 71 W/cm^2 ($P = 5$ W, $D = 3$ mm) with ice surface temperature $T_0 = 0.8\,^\circ$C, no significant vapor depression or evaporation was observed, since the maximum temperature at the surface of the melting pond $T_{peak} = 70\,^\circ$C remains below the evaporation temperature of water, resulting in a convex pond [Fig. 6(b)]. At a high power density of 454 W/cm^2 ($P = 32$ W, $D = 3$ mm) with ice surface temperature $T_0 = 0.6\,^\circ$C, a pronounced crater formed due to significant evaporation. At greater crater depths $d_{w-i}(t_{crater}) = 7$ mm, the melt pond maintains a concave shape over 40 s [Fig. 6(b)]. At medium power densities, under a laser intensity 284 W/cm^2 ($P = 20$ W, $D = 3$ mm) and ice surface temperature $T_0 = 0.3\,^\circ$C, the melt pond evolution is characterized by a transition from a concave to a convex profile.

Craters form only when the laser power is sufficiently high to induce intense evaporation. With increasing laser power, both the crater lifetime t_{crater} and its depth $d_{w-i}(t_{crater})$ increase [Figs. 6(c) and 6(d)]. Remarkably, the deeper crater [$d_{w-i}(t_{crater}) \geq 4$ mm] under high laser power inhibits the formation of a convex melt pool,

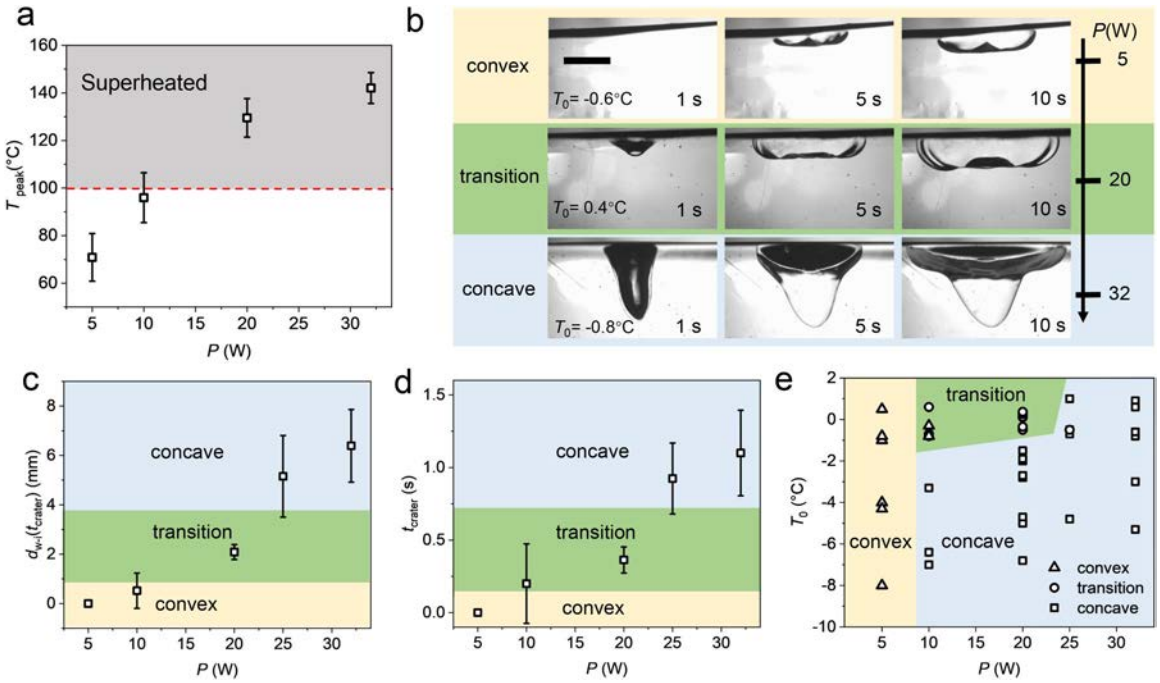

FIG. 6. The effect of laser power on melt pond. (a) Variation of the peak temperature at the melt pond surface T_{peak} with laser power. Ice at $T_0 = \pm 1\,^{\circ}\mathrm{C}$. Red dashed line for the vaporization temperature of water. (b) Side-view images of the melt pond formed by laser impacting ($P = 5, 20, 32$ W, $D_{laser} = 3$ mm) on the ice at the initial surface temperature ($0 \le T_0 \le 0.8\,^{\circ}\mathrm{C}$). Scale bar for 4 mm. In the convex-evolution region (yellow shaded), the melt pond retains a triangular-convex shape. In the transition-evolution region (green shaded), the melt pond transitions from concave to convex. In the concave-evolution region (blue shaded), the melt pond is concave. (c) t_{crater} at different P. (d) Melt pond depth, $d_{wi}(t_{crater})$, at t_{crater} for various P. (e) Phase diagram of melt pond shape (following 10 s) under varying laser powers P and ice initial surface temperatures T_0.

resembling the influence of low initial surface temperature T_0 on melt pond shape.

VII. PHASE DIAGRAM OF MELT POND

The shape of the melt pond can be controlled by adjusting the initial ice surface temperature T_0 and the laser power P. The phase diagram in Fig. 6(e) shows ice melt pond shape evolution depending on laser power P and initial ice surface temperature T_0. At a low power ($P \le 5$ W), the melt pond maintains a convex shape due to the thermocapillary effects in the thick water layer and the absence of evaporation. Conversely, at high power ($P \ge 30$ W), the recoil pressure from intense evaporation stabilizes a deep vapor crater, overcoming the influence of the pre-melting layer, resulting in a concave melt pool profile that is independent of the initial temperature T_0. Within the intermediate power range ($10 \le P \le 20$ W), the melt pond morphology evolution is sensitive to the existence of the pre-melted layer on the ice.

VIII. GROOVE-SHAPED MELT POND UNDER LASER SCANNING MODE

After investigating the stationary laser impacting on the ice, we proceed to explore melt pond sculpting by a scanning laser subjected to a relative linear horizontal translation speed (v_{trans}) along a linear axis beneath the fixed optical setup [Fig. 7(a)]. By means of a mirror with a focal length of 500 mm, the laser beam ($D = 3$ mm) is focused into a spot with $D = 1$ mm with a Gaussian-distribution intensity, and then irradiates the ice surface.

For $v_{trans} = 0.2$ mm/s, the melt pond becomes groove shaped with a groove depth $d_g = 2.5$ mm under a laser intensity of 284 W/cm^2 ($P = 20$ W, $D = 3$ mm, with ice surface temperature $T_0 = 0.8\,^{\circ}\mathrm{C}$) [Fig. 7(b), Multimedia view]. Here, a ridge is generated around the center of the groove, originating from thermocapillary convection near the laser beam. This groove depth ($d_g = 1.5$ mm) is reduced at a faster speed of $v_{trans} = 0.5$ mm/s due to weaker local laser energy deposition [Fig. 7(c), Multimedia view]. Correspondingly, the ridge becomes smaller or even disappears under higher v_{trans} and lower d_g, because the position of the laser beam translates so fast that the melt pond has insufficient time to be shaped by thermocapillary convection before experiencing subsequent cooling.

Qualitatively, the input energy of the scanning laser over length dl within the local dwelling time $[(dl)/v_{trans}]$ is $dQ_{in} = P(dl)/v_{trans}$, and the energy consumed by the melt pond is $Q_{melt} = \rho(L_m + c_p\Delta T)S_{cross}(dl)$, where $S_{cross} \propto d_g^2$ for the cross sectional area of the groove.[47] By balancing the energy $Q_{in} = Q_{melt}$, the following scaling is obtained:

$$d_g \propto {v_{trans}}^{-1/2}. \tag{5}$$

Indeed, this $-1/2$ scaling agrees well with the experimental measurements [Fig. 7(d)].

Additionally, under the irradiation of a focused high-intensity laser beam [Fig. 7(e)], the groove-shaped melt pond becomes more

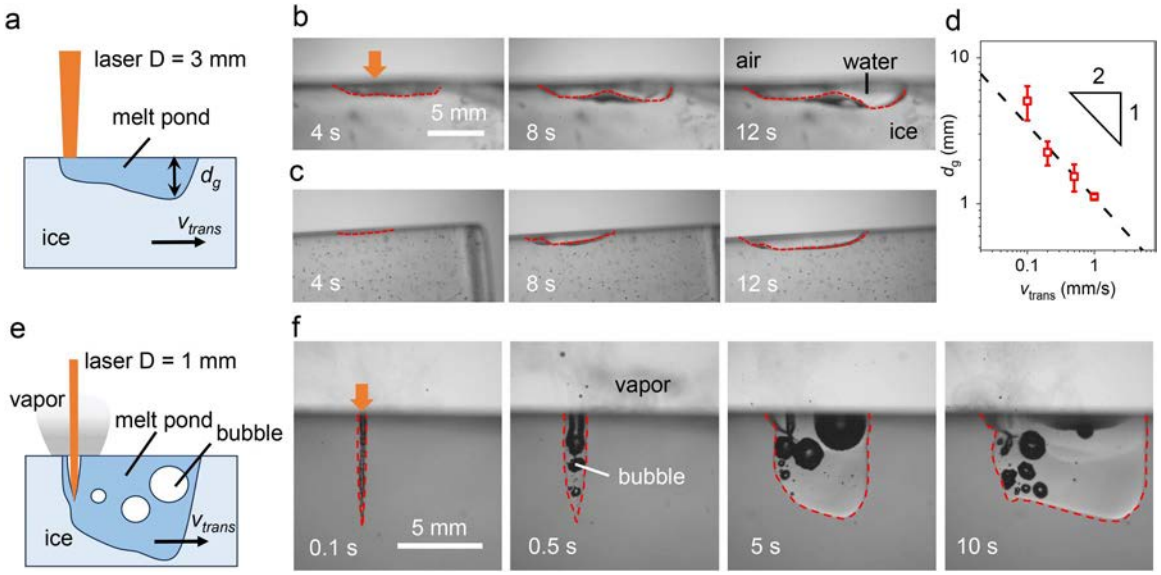

FIG. 7. Groove-shaped melt pond. (a) Sketch of the shaped melt pond formed by relative horizontal translation of the laser beam (beam size $D = 3$ mm). (b) and (c) Snapshots for laser ($P = 20$ W, $D = 3$ mm) at different translation speeds ($v_{trans} = 0.2, 0.5$ mm/s), corresponding to groove depths $d_g = 2.5, 1.5$ mm, respectively. (d) d_g follows a $-1/2$ scaling law with translation speed v_{trans}. (e) Sketch of deep ice penetration under strong laser intensity (focused beam size $D = 1$ mm). (f) Snapshots for focused laser ($P = 20$ W, $D = 1$ mm) at $v_{trans} = 0.5$ mm/s, resulting in deeper $d_g = 7.5$ mm, more visible vaporization, and production of bubbles ($T_0 \approx 0.8\,^{\circ}$C). Multimedia available online.

complex. At the laser intensity (2840 W/cm^2 with a spot diameter $D = 1$ mm), violent vaporization of ice or water into air subsequently causes the formation of a deeper crater with $d_g = 7.5$ mm. This crater then experiences instability, causing it to collapse and produce bubbles confined with the melt pond [Fig. 7(f), Multimedia view].

IX. NUMERICAL SIMULATIONS

To reveal the underlying physical mechanism of the melt pond morphology transition, we perform numerical simulations of the coupled equations for energy, momentum, and mass conservation, taking into account heat transfer and hydrodynamic flow, as well as phase change including both vaporization and melting due to laser heating. The computational domain and boundary conditions are schematically illustrated in Fig. S2, with detailed descriptions provided in supplementary material Note 2. The level-set model is implemented to capture the air–water interface, while the effective heat capacity method is applied to track the water–ice interface.

For laser impacting on the ice to form the melt pond, the governing equations for energy, momentum, and mass conservation are expressed as follows:

$$\rho c_p\left[\frac{\partial T}{\partial t} + \vec{\nabla}\cdot(\vec{u}T)\right] = \vec{\nabla}\cdot(k\vec{\nabla}T) + S_{\text{laser}} + Q_{\text{vap}}, \tag{6a}$$

$$\rho\left[\frac{\partial \vec{u}}{\partial t} + \vec{u}\cdot(\vec{\nabla}\cdot\vec{u})\right] = \vec{\nabla}\cdot\left[-pI + \mu\left(\vec{\nabla}\vec{u} + (\vec{\nabla}\vec{u})^T\right)\right] + \tau, \tag{6b}$$

$$\vec{\nabla}\cdot\vec{u} = \dot{m}\delta(\phi)\left(\frac{\rho_l - \rho}{\rho^2}\right). \tag{6c}$$

For energy conservation [Eq. (6a)], T denotes the temperature, t denotes time, $\rho(T)$ is the density, $c_p(T)$ is the effective heat capacity, $k(T)$ is the thermal conductivity, $S_{\text{laser}} = \frac{nP}{\pi R^2}e^{-\frac{nr^2}{R^2}}\delta(\phi)$ represents the heat source of laser deposition at the surface of ice/water with negligible reflection loss ($\approx$1%),[40] and $Q_{\text{vap}} = -L_v\dot{m}\delta(\phi)H(T_{\text{vap}})$ represents energy loss due to evaporation.

For mass [Eq. (6c)], both gas and liquid are considered as incompressible Newtonian fluids, but at the air–water interface, an additional term representing a local interfacial mass transfer source due to expansion upon liquid–gas phase change is introduced into the continuity equation [$\rho = \rho(T)$ is the temperature-dependent density of the different phase, and ρ_l is the water density in the liquid phase].

The mass flux of evaporation ($\dot{m}$) due to laser heating is given by

$$\dot{m} = \sqrt{\frac{m_0}{2\pi k_B}}\frac{p_{\text{sat}}(T)}{\sqrt{T}}, \tag{7}$$

where m_0 is the molecular weight of water, k_B is the Boltzmann constant, T_{vap} is the evaporation temperature, and $p_{\text{sat}}(T) = p_a\exp[\frac{\Delta H_v}{k_B T_{\text{vap}}}(1 - \frac{T_{\text{vap}}}{T})]$ is the saturated vapor pressure.

To solve the coupled equations for the three phases (gas, liquid, and solid), the level-set method is applied to describe the phase change process at the air–water interface,

$$\frac{\partial\phi}{\partial t} + \vec{u}\cdot\vec{\nabla}\phi - \dot{m}\delta(\phi)\left(\frac{1}{\rho}\right) = \gamma_{ls}\nabla\cdot\left[\varepsilon_{ls}\nabla\phi - \phi(1-\phi)\frac{\nabla\phi}{|\nabla\phi|}\right], \tag{8}$$

where a source term due to evaporation is added to track the air–water interface ($\phi = 0.5$). Also, an effective heat capacity method is employed to capture the phase change process at the water–ice interface ($f_l = 0.5$).

For momentum [Eq. (6b)], $\vec{u}$ is the velocity vector, p is the pressure, I is the identity matrix, μ is the dynamic viscosity, and τ is the stress including contributions from gravitational force, buoyancy force, the Darcy damping force, and surface tension force. More details about the numerical simulation are provided in the supplementary material.

To confirm the effect of the premelting liquid layer, we simulate two most extreme cases by introducing initial and boundary conditions. In the first case, the upper layer of ice is covered by a water layer with a thickness $h_0 = 0.3$ mm with initial surface temperature $T_0 = 5\,^{\circ}$C. Here, the temperature distribution in the initial water layer is assumed to be linear. The second case is bare ice with $T_0 = -10\,^{\circ}$C, $h_0 = 0$ mm (Multimedia view).

Figure 8(a) shows snapshots of the temperature distribution, velocity field, and water–ice interface in the melt pond with $T_0 = 5\,^{\circ}$C. Clearly, at a late stage (such as $t = 5$ s), recirculation flows—outward in the upper part of the melt pond and inward flow in the lower part—significantly shape the melting front or the water–ice interface, resulting in a transition from a concave profile to a convex contour [Fig. 8(c)]. Due to convective heat transfer, the isotherm lines are modified by the flows accordingly.

On the contrary, with $T_0 = -10\,^{\circ}$C, the thin water layer results in the melt pond maintaining a concave rather than a convex shape [Figs. 8(b) and 8(d)]. Figure 8(e) shows the dependence of the water layer thickness h_w on time for various T_0 in the simulation, consistent with the experiment.

To demonstrate the coupling of convective flows and heat transfer, Figs. 9(a) and 9(b) illustrate the horizontal velocity profile (v_x) and temperature (T) as a function of depth (h) at $r = -R/3$ inside the laser zone at $t = 0.3, 1, 3$ s with $T_0 = 5\,^{\circ}$C. Here, the region above the red dashed line is water, and the region below is ice. Initially, say at $t = 0.3$ s, owing to the constant heat flux of laser and small liquid thickness, a large temperature gradient of $O(10^2)$ K/mm in the melt pond indicates that the melt pond shape is dominated by heat conduction, which naturally generates the concave shape of the melt pond as expected. However, at a later time, as h_w increases to millimeter scale, thermal convection becomes important, and the temperature profile does not decrease monotonically with depth, but becomes complicated due to the inward recirculation flow. Consequently, the ice–water interface is distinctly shaped or sculpted by this convection.

Figures 9(c)–9(e) illustrate the evolution of temperature distribution of the air–water interface ($h = 0$ mm) and the internal layer ($h = 0.8$ mm) inside the melt pond $T_0 = 5\,^{\circ}$C. At the air–water interface [$h = 0$ mm, Fig. 9(c)], arising from constant heat flux under laser illumination, the temperature reaches its maximum at the center, and decays away from the center. However, in the internal layer [$h = 0.8$ mm, Figs. 9(d) and 9(e)], the temperature peak, at the center due to heat conduction from high temperature, gradually evolves into a temperature valley due to thermal convection, resulting in spatial variation of melting at the water–ice interface. Eventually, the concave water–ice interface of the melt pond transforms into a convex shape [Fig. 8(c)]. Naturally, when h_w remains thin, approximately 0.1 mm ($T_0 = 5\,^{\circ}$C), the water–ice interface maintains a concave shape [Fig. 8(d)].

It should be noted that the numerical model in this study does not adopt a fully conservative formulation, which may affect interface capturing in regions with drastic density variations, such as near the phase interface. For future work aiming at more quantitatively accurate simulations, implementing a fully conservative method is essential. In this regard, the hybrid approach for all-Mach-number multiphase flows[48] offers a particularly robust framework to address such challenges. Addressing these limitations will help bridge the gap between idealized laboratory studies and more complex natural or industrial scenarios.

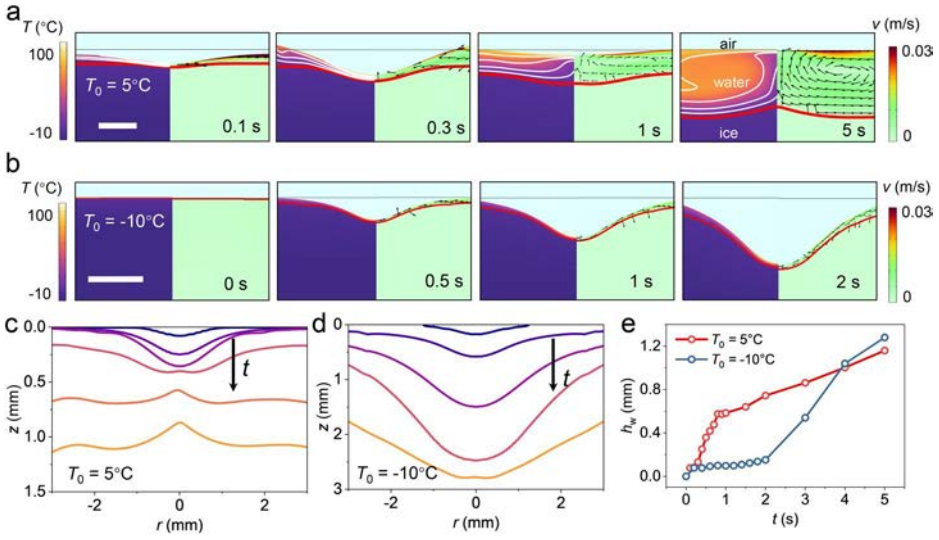

FIG. 8. Simulation of the convex/concave melt pond. (a) and (b) Snapshots of temperature distribution and velocity fields of melt pond at $T_0 = 5\,^{\circ}$C and $T_0 = -10\,^{\circ}$C, respectively. The white lines on the left correspond to the isotherm ($T = 10, 20, 50, 75\,^{\circ}$C from bottom to top), and the red lines to the ice–water interface. (c) Melt pond transition from concave to convex morphology at $T_0 = 5\,^{\circ}$C ($t = 0.1, 0.2, 0.3, 1, 3, 5$ s). (d) Concave melt pond morphology at $T_0 = -10\,^{\circ}$C ($t = 0.1, 0.5, 1, 2, 5$ s). (e) Thickness of the liquid layer (h_w) increasing with time at $T_0 = 5\,^{\circ}$C and $T_0 = -10\,^{\circ}$C. Multimedia available online.

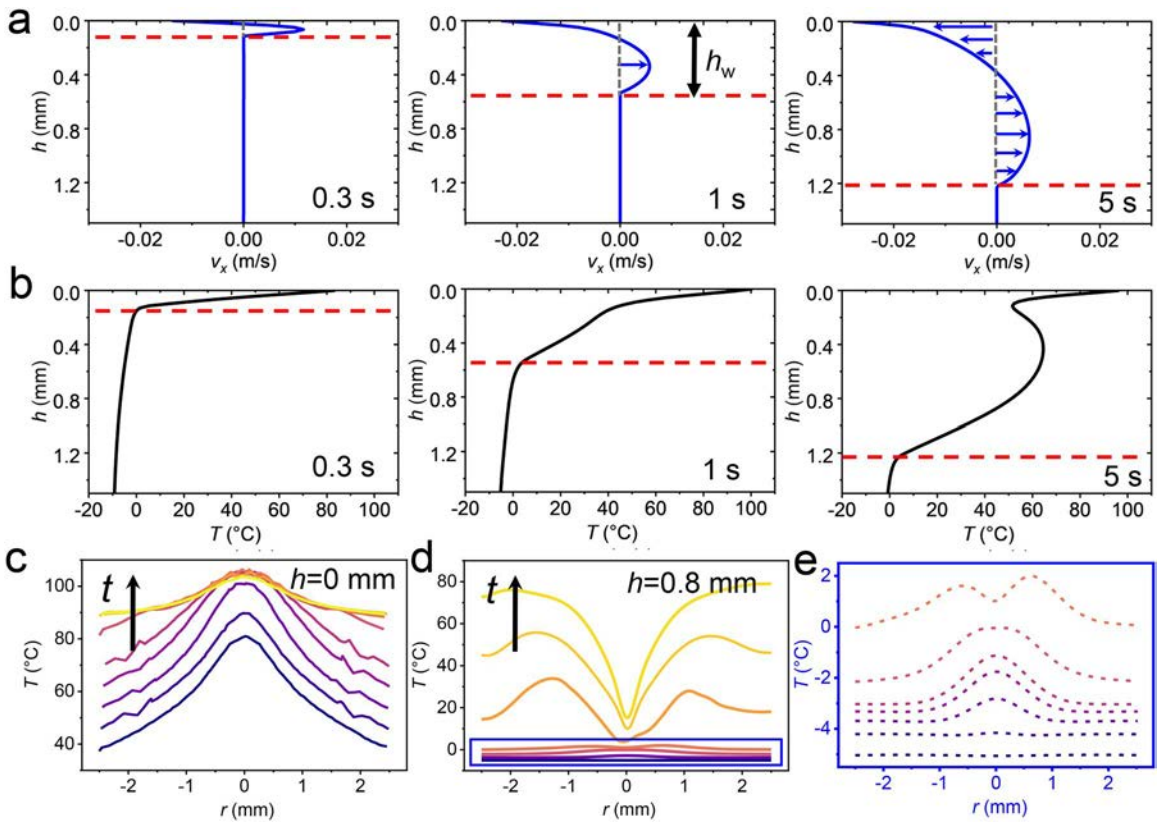

FIG. 9. Flow and temperature with water layer depth h from simulation of convex pond. (a) and (b) Horizontal velocity and temperature distributions as a function of the liquid depth (h) at $r = R/3 = 0.5$ mm at various times (at $t = 0.3, 1, 3$ s). Red dashed line correspond to water–ice interface. (c) For $h = 0$ mm, the evolution of radial temperature distribution in the air–water interface (at $t = 0.1, 0.3, 0.5, 1, 5$ s) with a central peak temperature, corresponding to the laser intensity. (d) and (e) For $h = 0.8$ mm, the temperature transitions from a central peak to a central valley arising from recirculation flows [at $t = 0.1, 0.3, 1, 3, 4, 5$ s in (d), and $t = 0.1, 0.3, 0.5, 1, 2$ s in (e)].

X. DISCUSSION AND OUTLOOK

We acknowledge several limitations in the present experimental study. First, temperature measurements were restricted to the surface using an infrared camera, which precludes direct access to the temperature distribution within the melt pool—a key factor to comprehensively understand coupled heat transfer and flow dynamics. Second, the initial thickness of the water film that forms on the ice surface upon melting was not directly measured experimentally. This parameter is critical for the validation of melt layer dynamics in simulations, and, consequently, its absence causes uncertainty in the quantitative comparison between experiments and simulations. Third, a number of experimental parameters—including the initial surface morphology of the ice sample and the laser beam size—were not systematically investigated in this work. A more systematic exploration of how these factors influence the critical conditions for morphological evolution (e.g., the transition criteria for interface shape) warrants future research.

The melting dynamics of ice are further complicated by saline environments, where dissolved salts depress the freezing point and alter seawater density gradients, accelerating ablation rates and reshaping ice morphology through double-diffusive convection.[49–52] These microscale phenomena—premelting layers and bubble dynamics—are closely analogous to natural ice–ocean interactions, such as marine ice cliff instability, a process where tall ice cliffs formed at marine-terminating glaciers become unstable and collapse.[53,54]

Our study of laser-irradiated ice melting provides critical insights into iceberg dynamics under radiative forcing, with direct relevance to global climate change. By linking microscale phase-change mechanisms to macroscale ice-sheet responses, these findings suggest promising avenues for future research into radiative strategies for mitigating freshwater loss and sea-level rise.

In real systems, multiple physical mechanisms may coexist and interact. Unlike recent observations of melt pond shape transitions dependent on its initial depth under solar radiation from a stable fully frozen state to another stable equilibrium state considering the natural convection induced by density difference,[35] here the melt pond formed under strong laser intensity is shaped by strong photo-thermocapillary convection, leading to an anomalous convex shape. Considering the dynamic Bond number $Bo = \frac{Ra}{Ma} = \frac{\Delta\rho}{\Delta\sigma} g l^2 \approx 10^{-4}$ here, which expresses the competition between Marangoni stress and gravity [with characteristic scale $l \sim O(10^{-3} \sim 10^{-2})$ m in this work and $l \sim O(10^{-1} \sim 10^{0})$ m in Ref. 35], the Marangoni convection is dominant in our system rather than Rayleigh convection.

Additionally, specific laser parameters (280 W/cm^2 intensity, 3 mm spot diameter) render the melt pond morphology highly responsive to variations in ice surface temperature. This sensitivity was obscured at higher laser power intensities, which are common in conventional laser processing and drilling applications. Under such conditions, disentangling the individual contributions of Marangoni stress, buoyancy, and bubble-induced stirring remains a non-trivial task and represents a complex multi-physics coupling that warrants further investigation.

In contrast, natural solar radiation (approximately 0.1 W/cm^2), characterized by its multispectral nature and significantly lower and uniform intensity, induces a considerably more gradual ablation process in ice. However, the physical picture differs significantly in natural systems characterized by much lower thermal inputs. If the magnitude of thermal Marangoni flows is comparable, it can be easily suppressed by the ubiquitous presence of trace surface contaminants.[55,56]

Therefore, while our high-energy system provides a clear platform to observe robust Marangoni-dominated patterns, applying these findings to quiescent natural settings—such as understanding transport processes at ice–ocean interfaces—requires careful consideration of the delicate balance between thermocapillarity and contamination effects. Future work bridging this gap between idealized high-flux experiments and realistic low-flux natural conditions will be valuable.

XI. CONCLUSION

In this work, by investigating ice-melting dynamics by irradiating transparent ice cubes with a mid-infrared 10.6 μm CO_2 laser, we have identified melt ponds transitioning from concave to anomalous convex morphologies, driven by thermal Marangoni flows at the ice–water interface. The melt pond pattern can be precisely controlled through premelting liquid layers (which favor convex patterns), laser power, or laser operation modes (e.g., scanning mode for groove-shaped channels). At elevated laser intensities, vaporization and bubble dynamics perturb ablation processes, replicating feedback mechanisms observed in natural ice–ocean systems, such as marine ice cliff instability. These findings not only demonstrate the potential of radiative interventions to modulate meltwater dynamics but also provide a deeper understanding of the ice-melting process by laser irradiation.

SUPPLEMENTARY MATERIAL

See the supplementary material for additional details on the model, simulations, and table in support of this manuscript.

AUTHOR DECLARATIONS

Conflict of Interest

The authors have no conflicts to disclose.

Author Contributions

Yuqi Li: Data curation (equal); Formal analysis (equal); Investigation (equal); Methodology (equal); Visualization (equal); Writing – original draft (equal). **Man Hu**: Investigation (equal); Supervision (equal); Visualization (equal); Writing – original draft (equal). **Feng Wang**: Investigation (supporting). **Li Chen**: Investigation (supporting). **Wenna Wu**: Investigation (supporting). **Peng Huo**: Investigation (supporting). **Xi Gu**: Investigation (supporting). **Daosheng Deng**: Conceptualization (equal); Project administration (equal); Supervision (equal); Writing – review & editing (equal).

DATA AVAILABILITY

The data that support the findings of this study are available from the corresponding author upon reasonable request.

REFERENCES

[1]C. Schoof and I. Hewitt, "Ice-sheet dynamics," Annu. Rev. Fluid Mech. **45**, 217–239 (2013).
[2]C. Cenedese and F. Straneo, "Icebergs melting," Annu. Rev. Fluid Mech. **55**, 377–402 (2023).
[3]A. F. Banwell, J. C. Burton, C. Cenedese, K. Golden, and J. Astrom, "Physics of the cryosphere," Nat. Rev. Phys. **5**, 446–449 (2023).
[4]M. Huss, "On the feasibility of glacier preservation," Nat. Water **2**, 606–607 (2024).
[5]J. L. Chen, C. R. Wilson, and B. D. Tapley, "Satellite gravity measurements confirm accelerated melting of Greenland Ice Sheet," Science **313**, 1958–1960 (2006).
[6]J. L. Chen, C. Wilson, D. Blankenship, and B. D. Tapley, "Accelerated Antarctic ice loss from satellite gravity measurements," Nat. Geosci. **2**, 859–862 (2009).
[7]R. Hugonnet, R. McNabb, E. Berthier, B. Menounos, C. Nuth, L. Girod, D. Farinotti, M. Huss, I. Dussaillant, F. Burn, and A. Kääb, "Accelerated global glacier mass loss in the early twenty-first century," Nature **592**, 726–731 (2021).
[8]N. R. Golledge, E. D. Keller, N. Gomez, K. A. Naughten, J. Bernales, L. D. Trusel, and T. L. Edwards, "Global environmental consequences of twenty-first-century ice-sheet melt," Nature **566**, 65–72 (2019).
[9]A. Witze, "Dramatic sea-ice melt caps tough Arctic summer," Nature **573**, 320–321 (2019).
[10]T. L. Edwards, S. Nowicki, B. Marzeion, R. Hock, H. Goelzer, H. Seroussi, N. C. Jourdain, D. A. Slater, F. E. Turner, C. J. Smith, C. M. McKenna, E. Simon, A. Abe-Ouchi, J. M. Gregory, E. Larour, W. H. Lipscomb, A. J. Payne, A. Shepherd, C. Agosta, P. Alexander, T. Albrecht, B. Anderson, X. Asay-Davis, A. Aschwanden, A. Barthel, A. Bliss, R. Calov, C. Chambers, N. Champollion, Y. Choi, R. Cullather, J. Cuzzone, C. Dumas, D. Felikson, X. Fettweis, K. Fujita, B. K. Galton-Fenzi, R. Gladstone, N. R. Golledge, R. Greve, T. Hattermann, M. J. Hoffman, A. Humbert, M. Huss, P. Huybrechts, W. Immerzeel, T. Kleiner, P. Kraaijenbrink, S. Le clec'h, V. Lee, G. R. Leguy, C. M. Little, D. P. Lowry, J. H. Malles, D. F. Martin, F. Maussion, M. Morlighem, J. F. O'Neill, I. Nias, F. Pattyn, T. Pelle, S. F. Price, A. Quiquet, V. Radić, R. Reese, D. R. Rounce, M. Rückamp, A. Sakai, C. Shafer, N. J. Schlegel, S. Shannon, R. S. Smith, F. Straneo, S. Sun, L. Tarasov, L. D. Trusel, J. Van Breedam, R. van de Wal, M. van den Broeke, R. Winkelmann, H. Zekollari, C. Zhao, T. Zhang, and T. Zwinger, "Projected land ice contributions to twenty-first-century sea level rise," Nature **593**, 74–82 (2021).
[11]C. R. Stokes, N. J. Abram, M. J. Bentley, T. L. Edwards, M. H. England, A. Foppert, S. S. R. Jamieson, R. S. Jones, M. A. King, J. T. M. Lenaerts, B. Medley, B. W. J. Miles, G. J. G. Paxman, C. Ritz, T. van de Flierdt, and P. L. Whitehouse, "Response of the East Antarctic ice sheet to past and future climate change," Nature **608**, 275–286 (2022).
[12]C. Amory, C. Buizert, S. Buzzard, E. Case, N. Clerx, R. Culberg, R. T. Datta, R. Dey, R. Drews, D. Dunmire, C. Eayrs, N. Hansen, A. Humbert, A. Kaitheri, K. Keegan, P. Kuipers Munneke, J. T. M. Lenaerts, S. Lhermitte, D. Mair, I. McDowell, J. Mejia, C. R. Meyer, E. Morris, D. Moser, F. M. Oraschewski, E. Pearce, S. de Roda Husman, B. Wouters, N. J. Schlegel, T. Schultz, S. B. Simonsen, C. M. Stevens, E. R. Thomas, M. Thompson-Munson, and N. Wever, "Firn on ice sheets," Nat. Rev. Earth Environ. **5**, 79–99 (2024).
[13]J. J. Li, Y. Liang, W. Li, N. Xu, B. Zhu, Z. Wu, X. Wang, S. Fan, M. Wang, and J. Zhu, "Protecting ice from melting under sunlight via radiative cooling," Sci. Adv. **8**, eabj9756 (2022).

[14]N. N. Cao, H. W. Chi, B. Zhu, H. X. Pang, C. Q. Ke, X. W. Zhang, J. Chen, and J. Zhu, "Challenges to materials for local glacier conservation," Nat. Water **3**, 251–255 (2025).
[15]L. Rubinstein, *The Stefan Problem* (American Mathematical Society, Providence, RI, 1971).
[16]S. H. Davis, *Theory of Solidification* (Cambridge University Press, 2001).
[17]C. Polashenski, D. K. Perovich, and Z. Courville, "The mechanisms of sea ice melt pond formation and evolution," J. Geophys. Res. **117**, C01001, https://doi.org/10.1029/2011JC007231 (2012).
[18]C. Polashenski, K. M. Golden, D. K. Perovich, E. Skyllingstad, A. Arnsten, C. Stwertka, and N. Wright, "Percolation blockage: A process that enables melt pond formation on first year arctic sea ice," J. Geophys. Res.: Oceans **122**, 413–440, https://doi.org/10.1002/2016JC011994 (2017).
[19]B. R. Esfahani, S. C. Hirata, S. Berti, and E. Calzavarini, "Basal melting driven by turbulent thermal convection," Phys. Rev. Fluids **3**, 053501 (2018).
[20]R. Lenormand, Z. Touboul, and C. Zarcone, "Numerical models and experiments on immiscible displacements in porous media," J. Fluid Mech. **189**, 165–187 (1988).
[21]C.-Y. Lai, J. Kingslake, M. G. Wearing, P.-H. C. Chen, P. Gentine, H. Li, J. J. Spergel, and J. M. van Wessem, "Vulnerability of Antarctica's ice shelves to meltwater-driven fracture," Nature **584**, 574–578 (2020).
[22]D. M. Chandler and A. Hubbard, "Widespread partial-depth hydrofractures in ice sheets driven by supraglacial streams," Nat. Geosci. **16**, 605–611 (2023).
[23]Y. Du, E. Calzavarini, and C. Sun, "The physics of freezing and melting in the presence of flows," Nat. Rev. Phys. **6**, 676–690 (2024).
[24]S. Weady, J. Tong, A. Zidovska, and L. Ristroph, "Anomalous convective flows carve pinnacles and scallops in melting ice," Phys. Rev. Lett. **128**, 044502 (2022).
[25]Z. Q. Wang, E. Calzavarini, C. Suna, and F. Toschi, "How the growth of ice depends on the fluid dynamics underneath," Proc. Natl. Acad. Sci. U. S. A. **118**, e2012870118 (2021).
[26]E. W. Hester, C. D. McConnochie, C. Cenedese, L.-A. Couston, and G. Vasil, "Aspect ratio affects iceberg melting," Phys. Rev. Fluids **6**, 023802 (2021).
[27]R. Yang, T. van den Ham, R. Verzicco, D. Lohse, and S. G. Huisman, "Circular objects do not melt the slowest in water," Phys. Rev. Fluids **9**, 083501 (2024).
[28]M. E. Wengrove, E. C. Pettit, J. D. Nash, R. H. Jackson, and E. D. Skyllingstad, "Melting of glacier ice enhanced by bursting air bubbles," Nat. Geosci. **16**, 871–876 (2023).
[29]J. Tyndall, "On some physical properties of ice," Proc. R. Soc. London, Ser. A **9**, 76–80 (1859).
[30]A. A. Lacey, M. G. Hennessy, P. Harvey, and R. F. Katz, "Mathematical modelling of Tyndall star initiation," Eur. J. Appl. Math. **26**, 615–645 (2015).
[31]S. Takeya, "Growth of internal melt figures in superheated ice," Appl. Phys. Lett. **88**, 074103 (2006).
[32]S. Mae, "The freezing of small Tyndall figures in ice," J. Glaciol. **17**, 111–116 (1976).
[33]S. G. Preis, H. Chayet, A. Katz, V. Yashunsky, A. Kaner, S. Ullman, and I. Braslavsky, "Labyrinth ice pattern formation induced by near-infrared irradiation," Sci. Adv. **5**, eaav1598 (2019).
[34]P. Popovic, B. B. Cael, M. Silber, and D. S. Abbot, "Simple rules govern the patterns of Arctic Sea ice melt ponds," Phys. Rev. Lett. **120**, 148701 (2018).
[35]R. Yang, C. J. Howland, H. R. Liu, R. Verzicco, and D. Lohse, "Bistability in radiatively heated melt ponds," Phys. Rev. Lett. **131**, 234002 (2023).
[36]K. Y. Vinnikov, A. Robock, R. J. Stouffer, J. E. Walsh, C. L. Parkinson, D. J. Cavalieri, J. F. B. Mitchell, D. Garrett, and V. F. Zakharov, "Global warming and northern hemisphere sea ice extent," Science **286**, 1934–1937 (1999).
[37]T. Sakurai, H. Chosrowjan, T. Somekawa, M. Fujita, H. Motoyama, O. Watanabe, and Y. Izawa, "Studies of melting ice using CO_2 laser for ice drilling," Cold Reg. Sci. Technol. **121**, 11–15 (2016).
[38]Z. Zhen, K. Shao, M. Song, L. Zhang, L. Shen, and L. Pekar, "An experimental study on the effect of CO_2 laser powers on melting characteristics of clear ice—Part I: Horizontal irradiation," Appl. Therm. Eng. **248**, 123208 (2024).
[39]Z. Zekang, S. Mengjie, S. Jun, Z. Long, and Z. Xuan, "An experimental study on the effect of CO_2 laser powers on melting characteristics of ice with trapped air bubbles under vertical irradiation," Appl. Therm. Eng. **236**, 121533 (2024).
[40]G. M. Hale and M. R. Querry, "Optical constants of water in the 200-nm to 200-μm wavelength region," Appl. Opt. **12**, 563 (1973).
[41]S. Warren, "Optical constants of ice from the ultraviolet to the microwave," Appl. Opt. **23**, 1206–1225 (1984).
[42]S. G. Warren and R. E. Brandt, "Optical constants of ice from the ultraviolet to the microwave: A revised compilation," J. Geophys. Res. **113**, D14220, https://doi.org/10.1029/2007JD009744 (2008).
[43]V. F. Petrenko and R. W. Whitworth, *The Physics of Ice* (Oxford University Press, 1999).
[44]S. Anand, A. Engelbrecht, and D. McGloin, "Optically written optofluidic ice channels," J. Opt. **13**, 044005 (2011).
[45]F. Wang, L. Chen, Y. Q. Li, P. Huo, X. Gu, M. Hu, and D. S. Deng, "Self-lifting droplet driven by the solidification-induced solutal Marangoni flow," Phys. Rev. Lett. **132**, 014002 (2024).
[46]B. Slater and A. Michaelides, "Surface premelting of water ice," Nat. Rev. Chem. **3**, 172–188 (2019).
[47]M. Hu, F. Wang, L. Chen, P. Huo, Y. Q. Li, G. Xi, K. L. Chong, and D. S. Deng, "Near-infrared-laser-navigated dancing bubble within water via a thermally conductive interface," Nat. Commun. **13**, 5749 (2022).
[48]X. Deng, B. Xie, O. K. Matar, and P. Boivin, "A novel hybrid approach for accurate simulation of compressible multi-component flows across all-Mach number," J. Comput. Phys. **540**, 114282 (2025).
[49]H. E. Huppert and J. S. Turner, "On melting icebergs," Nature **271**, 46–48 (1978).
[50]H. E. Huppert and J. S. Turner, "Ice blocks melting into a salinity gradient," J. Fluid Mech. **100**, 367–384 (1980).
[51]C. D. McConnochie and R. C. Kerr, "The effect of a salinity gradient on the dissolution of a vertical ice face," J. Fluid Mech. **791**, 589–607 (2016).
[52]R. Yang, C. J. Howland, H. R. Liu, R. Verzicco, and D. Lohse, "Ice melting in salty water: Layering and non-monotonic dependence on the mean salinity," J. Fluid Mech. **969**, R2 (2023).
[53]A. J. Crawford, D. I. Benn, J. Todd, J. A. Astrom, J. N. Bassis, and T. Zwinger, "Marine ice-cliff instability modeling shows mixed-mode ice-cliff failure and yields calving rate parameterization," Nat. Commun. **12**, 2701 (2021).
[54]J. N. Bassis, B. Berg, A. J. Crawford, and D. I. Benn, "Transition to marine ice cliff instability controlled by ice thickness gradients and velocity," Science **372**, 1342–1344 (2021).
[55]J. Yu, Z. Pan, and J. A. Weibel, "Transition of buoyancy-driven flow from an axisymmetric to non-axisymmetric vortex inside an evaporating sessile droplet," J. Fluid Mech. **997**, A47 (2024).
[56]S. Dash, A. Chandramohan, J. A. Weibel, and S. V. Garimella, "Buoyancy-induced on-the-spot mixing in droplets evaporating on nonwetting surfaces," Phys. Rev. E **90**, 062407 (2014).